

VEHICLE DYNAMICS MODELING AND ELECTRONIC STABILITY PROGRAM/ ACTIVE FRONT STEERING SLIDING MODE INTEGRATED CONTROL

Xiaobin Fan  and Zixiang Zhao

ABSTRACT

Chassis integrated control can significantly improve vehicle handling stability and comfort. Because of the complexity of the problem, it has attracted significant research attention. We built a vehicle nonlinear dynamic model with multi-degree freedom, including body movement, wheel movement, and electronically controlled hydraulic power steering system. We compared the magic formula tire model, Dugoff tire model, brush tire model, and LuGre dynamic friction tire model and steady model. The precision of the model was verified by a comparison between simulation results and the real vehicle test results. Then, based on the vehicle dynamics model, an AFS (active front steering) controller was designed based on sliding mode variable structure control, and an AFS and ESP (electronic stability program) integrated coordination controller was proposed. Finally, based on the nonlinear tire model and multi-DOF (degree of freedom) vehicle model, sinusoidal and step steering angle input simulation analysis was proposed on different road friction coefficients. The results show that the vehicle has better response characteristics with coordinated control strategy when compared with AFS and ESP only control. The evidence suggests that the proposed integrated control system in this paper can improve vehicle stability and safety.

Key Words: Vehicle dynamics, tire model, active steering, stability control, coordinated control, coefficient of adhesion.

1. INTRODUCTION

Active front steering (AFS) and electronic stability program (ESP) are active safety devices for vehicles to improve vehicle handling and stability. In the linear range of the tire lateral force, the vehicle can intervene more directly and quickly through the AFS, and the energy required and tire wear is so small as to be difficult for a driver to detect. This differs from the nonlinear range of automobile tires, where the control effect of ESP is obvious.

Aripin proposed a composite nonlinear feedback technique for yaw tracking control of an AFS system with the objective to improve the transient performance of yaw rate response. The designed controller is evaluated using a J-turn cornering manoeuvre condition in computer simulation [1]. Zheng proposed an algorithm that achieved the decoupling of the lateral and yaw motion of a vehicle and the vehicle's yaw damping simultaneously by the feedback

of both yaw rate and front steering angle [2]. Krishna proposed a fuzzy logic-based yaw stability controller for AFS of a four-wheeled road vehicle by using a steer-by-wire system. The proposed control system takes the yaw rate error, the steering angle given by the driver, and the vehicle body side slip angle as inputs to calculate the additional steering angle as output for stabilizing the yaw moment of the vehicle [3]. Yim proposed an optimum distribution method for yaw moment for use with unified chassis control with limitations on the AFS angle. This method derived an optimum longitudinal/lateral force using the Karush-Kuhn-Tucker optimality condition, and a simulation was performed to validate the proposed method [4]. Nam proposed a robust yaw stability control based on AFS control for in-wheel-motored electric vehicles with a steer-by-wire system. The proposed control system consisted of an inner-loop controller (the steering angle-disturbance observer), which rejects an input steering disturbance by feeding a compensation steering angle, and an outer-loop tracking controller to achieve control performance and stability [5]. Fujimoto proposed a method for obtaining longitudinal and lateral-force distributions based on least-squares solutions of the equations of longitudinal, lateral, and yawing motions. He also proposed a lateral-force control method using tire lateral force sensors, active front and rear steering systems, and a direct yaw moment control (DYC) method for enhancing the yaw-rate control performance [6]. Cairano proposed a

Manuscript received August 30, 2017; revised February 7, 2018; accepted March 18, 2018.

The authors are with School of Mechanical and Power Engineering, Henan Polytechnic University, Jiaozuo 454000, China.

Xiaobin Fan is the corresponding author (e-mail: fanxiaobin@hpu.edu.cn).

This research was supported by Key Scientific Research Project of Henan Province (No. 17A580003), Key Scientific and Technological Project of Henan Province (No. 172102210022), Natural Science Foundation of Henan Province of China (No. 182300410265) and National Undergraduate Training Program for Innovation and Entrepreneurship (No. 201710460096).

model predictive control strategy to coordinate the actuators and formulated the vehicle dynamics with respect to the tire slip angles, using a piecewise affine approximation of the tire force characteristics [7]. Elmarakbi investigated the influence of integration of vehicle dynamics control systems by proposing new control architecture to integrate the braking, steering, suspension, and driveline [8]. Choi proposed a control architecture that simultaneously utilized AFS and differential braking for vehicle lateral stability while minimizing longitudinal perturbations. This control scheme was based on model predictive control using the extended bicycle model that captures the lagged characteristics of tire forces and actuators [9]. Guo proposed an integrated control system by coordinating control of AFS and ESP, including a coordinated controller in the upper layer and two subsystem controllers in the lower layer [10]. Marar proposed a sliding mode controller utilized for yaw rate reference tracking and side slip stability. A disturbance observer was combined with a sliding mode controller to make robust the performance in the presence of parametric uncertainties [11]. Saikia used a sliding-mode control methodology in the upper-level control in order to generate the corrective steering wheel angle and yaw moment. The yaw moment was realized through braking between appropriate wheels in the second-level control. Stability of the sliding mode controller was proved using Lyapunov criterion [12]. Yang proposed integrating the control systems of AFS and DYC using a dynamic inversion control law [13]. Sun designed a fuzzy control algorithm integrated direct yaw moment control and AFS with lateral velocity estimation [14]. It is difficult to design a robust controller when the system parameters are unknown. The control algorithm of linear matrix inequality (LMI)-based fractional-order surface for sliding-mode controller of a class of uncertain fractional-order nonlinear systems (FO-NSs) has a good effect [15,16]. Ghanavati considered scenarios wherein a group of malicious vehicles on a highway perform a cooperative attack with the motive of creating undesirable wave effects among other vehicles on the highway [17]. In order to improve vehicle lateral dynamics performance with active steering and active braking, Solmaz presented a robust controller design methodology for vehicle rollover prevention utilizing active steering [18]. Chiu designed differential-braking-based rollover controllers to keep the value of the Load Transfer Ratio LTR_d below a certain level, and the controllers yielded robustness to variations in vehicle speed [19].

Although scholars have carried out extensive research on the implementation of coordinated control, they do not focus on implementation of the algorithm and real vehicle verification. The robustness of the control algorithm is not satisfactory. There are few studies that examine the dynamic friction characteristics of the tire. So, in this study a precise

vehicle high-dimensional nonlinear dynamic model and a tire dynamic friction model were established. AFS, ESP and coordinated control algorithm were designed. The results show that a coordinated control algorithm has a better control effect.

II. VEHICLE DYNAMICS MODELING

In this section, the vehicle nonlinear multi-degree of freedom dynamics model is developed, which includes body, steering system, braking system, and tire subsystem model [20].

2.1 Vehicle body dynamics model

The body dynamics model was established as Fig. 1, which includes longitudinal motion u , lateral motion v , yaw motion r and roll motion ϕ . The differential equations of motion for the four degrees of freedom are listed as follows.

$$m\dot{u} = mvr + F_{xfl} + F_{xfr} + F_{xrl} + F_{xrr} - \frac{1}{2}C_d A_f \rho_a u^2 \quad (1)$$

$$m\dot{v} + m_s e \dot{p} = -mur + F_{yfl} + F_{yfr} + F_{yrl} + F_{yrr} \quad (2)$$

$$I_{zz}\dot{r} - I_{xzs}\dot{p} = a(F_{yfl} + F_{yfr}) - b(F_{yrl} + F_{yrr}) + \frac{T_w}{2}(F_{xfl} + F_{xrl} - F_{xfr} - F_{xrr}) \quad (3)$$

$$I_{xxs}\dot{p} + m_s e \dot{v} - I_{xzs}\dot{r} = -m_s eur + m_s ge \sin \phi - K_\phi \phi - C_\phi \dot{\phi} \quad (4)$$

$$\dot{\phi} = p \quad (5)$$

where, m is the total mass of vehicle, [kg]; C_d is drag coefficient; A_f is front face area, [m²]; ρ_a is air density, [kg/m³]; m_s is sprung mass, [kg]; e is distance between the center of mass of spring load and the axis of roll, [m]; I_{zz} is yaw moment of inertia, [kg·m²]; I_{xzs} is yaw roll inertial product, [kg·m²]; a is distance between center of mass and front axle, [m]; b is distance between center of mass and rear axle, [m]; T_w is wheel-base, $T_w = T_f = T_r$, [m]; I_{xxs} is moment of inertia around the roll axis, [kg·m²]; K_ϕ is roll stiffness coefficient, [N m/rad]; C_ϕ is roll damping coefficient, [N/rad].

Body longitudinal force F_{xi} and lateral force F_{yi} are as follows.

$$F_{xi} = F_{ti} \cos \delta_i - F_{si} \sin \delta_i \quad (6)$$

$$F_{yi} = F_{ti} \sin \delta_i + F_{si} \cos \delta_i \quad (7)$$

where, $i = fl, fr, rl, rr$. F_{ti} is the longitudinal force of the tire, F_{si} is the lateral force of the tire. They are calculated

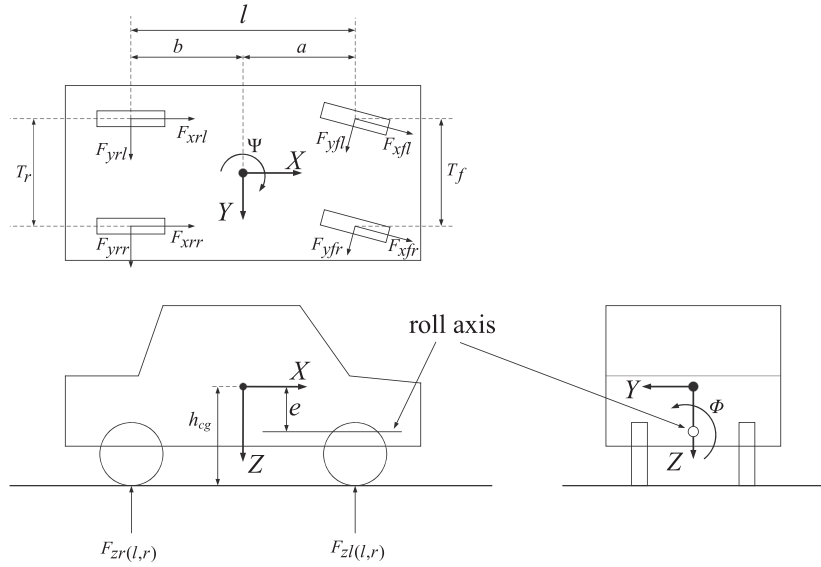


Fig. 1. Vehicle body dynamics model.

according to the tire model. δ_i is steering angle for wheels, which is as follows.

$$\delta_{fl} = \delta_{fr} = \delta + k_{rsf} \phi \quad (8)$$

$$\delta_{rl} = \delta_{rr} = k_{rsr} \phi \quad (9)$$

where, δ is the theoretical steering angle of the front wheel, k_{rsf} is the roll steering coefficient of the front wheel, k_{rsr} is the rear wheel roll steering coefficient.

The vertical forces F_{zi} of each wheel are as follows.

$$F_{zfl} = \frac{mg}{2} \left[\frac{b}{l} - \frac{\dot{u} - vr h_{cg}}{g} + R_{rsf} \left(\frac{h_{cg} A_y}{T_w g} - \frac{m_s e}{m T_w} \sin \phi \right) \right] \quad (10)$$

$$F_{zfr} = \frac{mg}{2} \left[\frac{b}{l} - \frac{\dot{u} - vr h_{cg}}{g} - R_{rsf} \left(\frac{h_{cg} A_y}{T_w g} - \frac{m_s e}{m T_w} \sin \phi \right) \right] \quad (11)$$

$$F_{zrl} = \frac{mg}{2} \left[\frac{a}{l} + \frac{\dot{u} - vr h_{cg}}{g} + (1 - R_{rsf}) \left(\frac{h_{cg} A_y}{T_w g} - \frac{m_s e}{m T_w} \sin \phi \right) \right] \quad (12)$$

$$F_{zrr} = \frac{mg}{2} \left[\frac{a}{l} + \frac{\dot{u} - vr h_{cg}}{g} - (1 - R_{rsf}) \left(\frac{h_{cg} A_y}{T_w g} - \frac{m_s e}{m T_w} \sin \phi \right) \right] \quad (13)$$

where, h_g is centroid ground height, m; l is wheelbase, m; R_{rsf} is the ratio of the front axle roll stiffness to the total roll stiffness; A_y is lateral acceleration, and $A_y = \dot{v} + ur + \frac{m_s}{m} \dot{e}p$.

The speed of the vehicle in the world coordinate system is as follows.

$$\dot{X} = u \cos \Psi - v \sin \Psi \quad (14)$$

$$\dot{Y} = u \sin \Psi + v \cos \Psi \quad (15)$$

where, Ψ is the angle between the longitudinal axis of the body and the X axis of the world coordinate system.

2.2 Wheel dynamics model

The dynamic equations of the driving wheel are as follows.

$$\dot{\omega}_i = \frac{1}{I_{wi}} [T_i - R F_{ti} - T_{brki} - d_i F_{zi}] \quad (16)$$

where, R is wheel rolling radius. I_{wi} is wheel equivalent moment of inertia, $I_{wi} = I_t + \frac{1}{2} \zeta_j^2 \eta_j I_e$. I_t is wheel inertia. I_e is Engine inertia. ζ_j is total drive ratio of Powertrain. η_j is transmission efficiency. T_i is input drive torque. T_{brki} is braking torque. d_i is offset of wheel normal force.

For the non-driving wheel, the wheel dynamics equation is as follows.

$$\dot{\omega}_i = \frac{1}{I_{wi}} [-R F_{ti} - T_{brki} - d_i F_{zi}] \quad (17)$$

where, $I_{wi} = I_t$.

The side slip angles of each wheel are as follows.

$$\alpha_{fl} = \delta_{fl} - \arctan\left(\frac{v + ar}{u + \frac{1}{2}T_w r}\right) \quad (18)$$

$$\alpha_{fr} = \delta_{fr} - \arctan\left(\frac{v + ar}{u - \frac{1}{2}T_w r}\right) \quad (19)$$

$$\alpha_{rl} = \delta_{rl} + \arctan\left(\frac{br - v}{u + \frac{1}{2}T_w r}\right) \quad (20)$$

$$\alpha_{rr} = \delta_{rr} + \arctan\left(\frac{br - v}{u - \frac{1}{2}T_w r}\right) \quad (21)$$

The longitudinal slip ratio of each wheel is: $i_s = 1 - \frac{U_{ti}}{R\omega_i}$ (under acceleration) or $i_s = 1 - \frac{R\omega_i}{U_{ti}}$ (under braking).

The longitudinal speed of each wheel center is as follows.

$$U_{fl} = \left(u + \frac{1}{2}T_w r\right) \cos\delta_{fl} + (v + ar) \sin\delta_{fl} \quad (22)$$

$$U_{fr} = \left(u - \frac{1}{2}T_w r\right) \cos\delta_{fr} + (v + ar) \sin\delta_{fr} \quad (23)$$

$$U_{rl} = \left(u + \frac{1}{2}T_w r\right) \cos\delta_{rl} - (br - v) \sin\delta_{rl} \quad (24)$$

$$U_{rr} = \left(u - \frac{1}{2}T_w r\right) \cos\delta_{rr} - (br - v) \sin\delta_{rr} \quad (25)$$

2.3 Electronically controlled hydraulic power steering system model

Fig. 2. is the schematic diagram of the electro-hydraulic power steering system. Fig. 3. is the speed sensitive electro-hydraulic power steering characteristic curve of the studied vehicle [21]. The dynamic equations of the steering system are as follows.

$$I_w \ddot{\theta}_w = T_w - B_w(\dot{\theta}_w - \dot{\theta}_g) - K_w(\theta_w - \theta_g) \quad (26)$$

$$B_w(\dot{\theta}_w - \dot{\theta}_g) + K_w(\theta_w - \theta_g) - B_p(\dot{\theta}_g - \dot{\theta}_p) - K_p(\theta_g - \theta_p) = 0 \quad (27)$$

$$I_p \ddot{\theta}_p = B_p(\dot{\theta}_g - \dot{\theta}_p) + K_p(\theta_g - \theta_p) - F_p R_p \quad (28)$$

$$M_0 \ddot{X}_0 = F_p + F_0 - F_t - B_0 \dot{X}_0 - K_0 X_0 \quad (29)$$

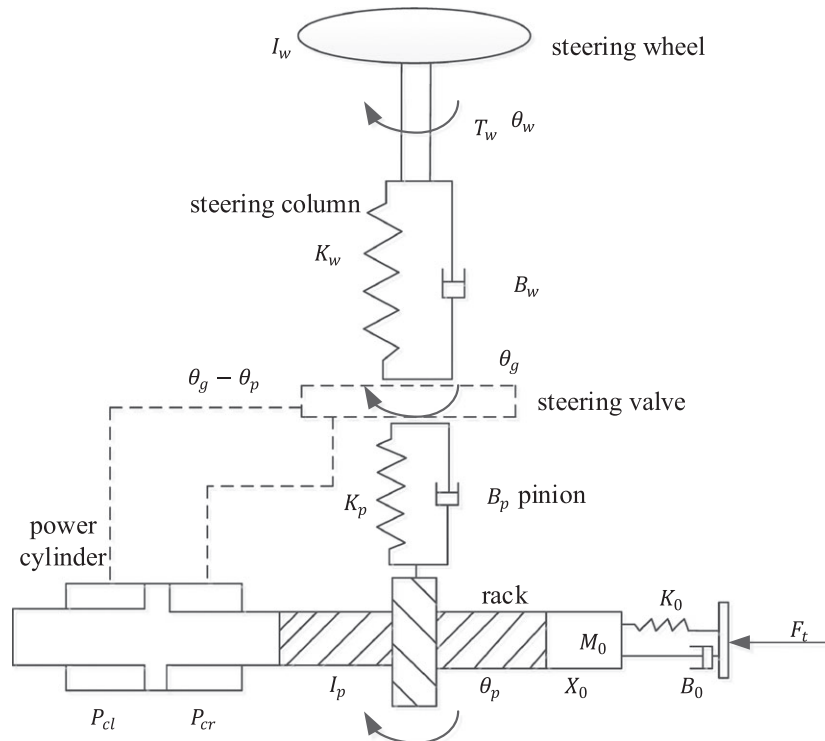


Fig. 2. Electric hydraulic power assisted steering.

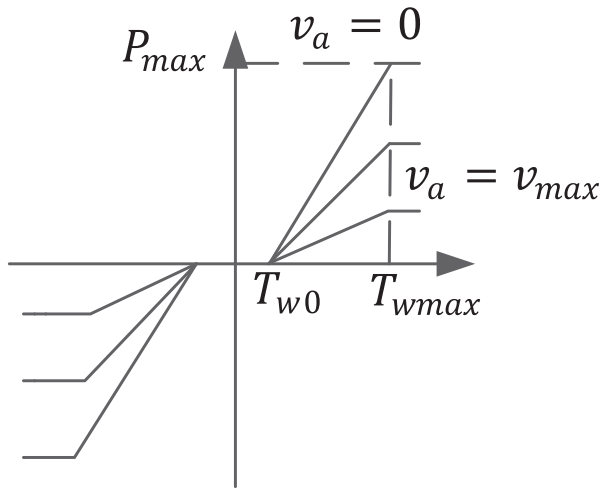


Fig. 3. Power steering characteristics.

$$F_0 = A_m(P_{cl} - P_{cr}) \quad (30)$$

$$X_0 = R_p \theta_p \quad (31)$$

where, I_w is inertia moment of steering wheel and steering column. T_w is steering wheel input torque. I_p is pinion moment of inertia. K_w and B_w are linear stiffness and linear damping coefficient of steering wheel and steering column. K_p and B_p are linear stiffness and linear damping coefficient of pinion. θ_w , θ_g and θ_p are steering wheel angular displacement, input shaft angular displacement, and pinion angular displacement. R_p is effective radius of pinion. M_0 is rack quality. X_0 is rack displacement. K_0 and B_0 are rack stiffness and damping coefficient. A_m is piston sectional area. F_b , F_p and F_0 are the forces acting on the rack of the road, pinion, and booster cylinder, $F_t = F_x \sin \delta + F_y \cos \delta$. In Fig. 4., F_x and F_y are tire longitudinal and lateral forces.

P_{cr} and P_{cl} are the pressure on the left and right sides of the piston. Hydraulic assistance is characterized by Fig. 3.

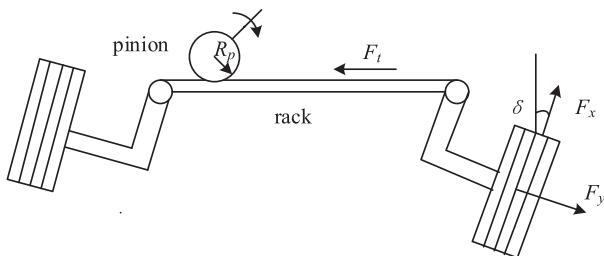


Fig. 4. Sketch of force acting on rack.

$$P = \begin{cases} 0 & 0 \leq T_w < T_{w0} \\ K(v) \cdot (T_w - T_{w0}) & T_{w0} \leq T_w < T_{wmax} \\ P_{max} & T_w \geq T_{wmax} \end{cases} \quad (32)$$

where, $K(v)$ is the coefficient of speed induction, it usually decreases as the speed increases. T_{w0} is the steering wheel input torque that starts when the power is turned on, $T_{w0} = 1$ N·m. T_{wmax} is Max input torque of steering wheel, $T_{wmax} = 7$ N·m. P_{max} is the maximum assist pressure determined according to the maximum turning resistance moment during the local steering, Pa.

2.4 Tire dynamic friction model

The tire's mechanical properties have important influence on vehicle handling stability, braking safety, and ride comfort. The development of modern automobile dynamics needs to establish an accurate tire model that reflects the tire's physical essence, but also establishes the mathematical model of the vehicle to meet the different aspects.

(1) Dugoff tire model

The Dugoff model is simple, and the longitudinal slip, side slip, and combined working conditions are better in linear range. The main drawback is that the torque is not considered and the accuracy in the nonlinear range is poor. In the model, the lateral force F_s and the longitudinal force F_t are as follows [22].

$$F_s = \frac{C_a \tan \alpha}{1 - i_s} f(S) \quad (33)$$

$$F_t = \frac{C_i i_s}{1 - i_s} f(S) \quad (34)$$

where, C_a is the cornering stiffness of the tire. C_i is tire longitudinal stiffness.

$$S = \frac{\mu F_z [1 - \varepsilon_r u \sqrt{i_s^2 + \tan^2 \alpha}] (1 - i_s)}{2 \sqrt{C_i^2 i_s^2 + C_a^2 \tan^2 \alpha}} \quad (35)$$

$$f(S) = \begin{cases} S(2 - S) & \text{if } S < 1 \\ 1 & \text{if } S > 1 \end{cases}$$

where, ε_r is pavement adhesion reduction factor.

(2) Magic formula tire model

The magic formula tire model was put forward by Pacejka [23], which simulated the tire test data in the form of a trigonometric function combination, the tire model put forward a set of the same form and expression for tire longitudinal force, lateral force, and aligning torque. The

tire model has high precision and is suitable for programming. Fig. 5 is a schematic diagram of model parameters and longitudinal slip-sideslip definitions.

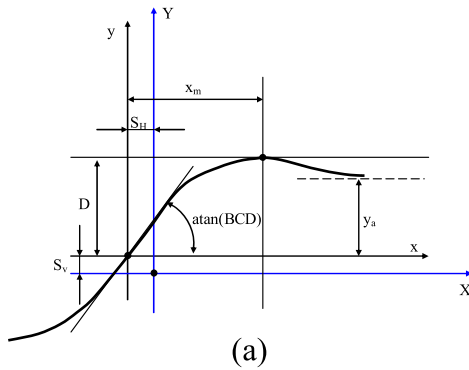
In the model, when the tire side slip angle α , camber angle γ , wheel longitudinal slip rate κ , and vertical load F_z are known, the longitudinal force F_{x0} under the pure longitudinal slip and the lateral force F_{y0} under the pure cornering condition can be expressed as follows respectively.

$$\begin{aligned} F_{x0} &= f_x(\kappa, \gamma, F_z) \\ &= D_x \sin[C_x \arctan\{B_x \kappa_x - E_x(B_x \kappa_x - \arctan(B_x \kappa_x))\}] \\ &\quad + S_{Vx} \end{aligned} \quad (36)$$

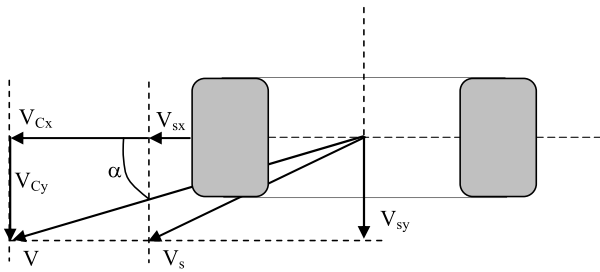
$$\begin{aligned} \kappa_x &= \kappa + S_{Hx} F_{y0} = f_y(\alpha, \gamma, F_z) \\ &= D_y \sin[C_y \arctan\{B_y \alpha_y - E_y(B_y \alpha_y - \arctan(B_y \alpha_y))\}] \\ &\quad + S_{Vy} \alpha_y = \alpha + S_{Hy} \end{aligned} \quad (37)$$

Longitudinal force and lateral force under combined condition of longitudinal slip and side slip are as follows.

$$\begin{aligned} F_x &= D_{xa} \sin[C_{xa} \arctan\{B_{xa} \alpha_s - E_{xa}(B_{xa} \alpha_s - \arctan(B_{xa} \alpha_s))\}] \alpha_s \\ &= \alpha + S_{Hxa} \end{aligned} \quad (38)$$



(a)



(b)

Fig. 5. Magic formula curve. [Color figure can be viewed at wileyonlinelibrary.com]

$$\begin{aligned} F_y &= D_y \sin[C_{y\kappa} \arctan\{B_{y\kappa} \kappa_s - E_{y\kappa}(B_{y\kappa} \kappa_s - \arctan(B_{y\kappa} \kappa_s))\}] \\ &\quad + S_{Vy\kappa} \kappa_s = \kappa + S_{Hy\kappa} \end{aligned} \quad (39)$$

(3) Tire brush model

The tire model consists of a series of flexible bristles that are attached to a rigid base (rim) [24]. These bristles can withstand vertical loads and produce longitudinal and lateral forces on the tire. The tire ground area is $2a$, as shown in Figs 6 and 7.

The pressure distribution function is as follows.

$$\sigma_z(x) = \frac{6F_z}{2a} \frac{x}{2a} \left(1 - \frac{x}{2a}\right) \quad (40)$$

(a) Longitudinal force f_x under pure longitudinal slip

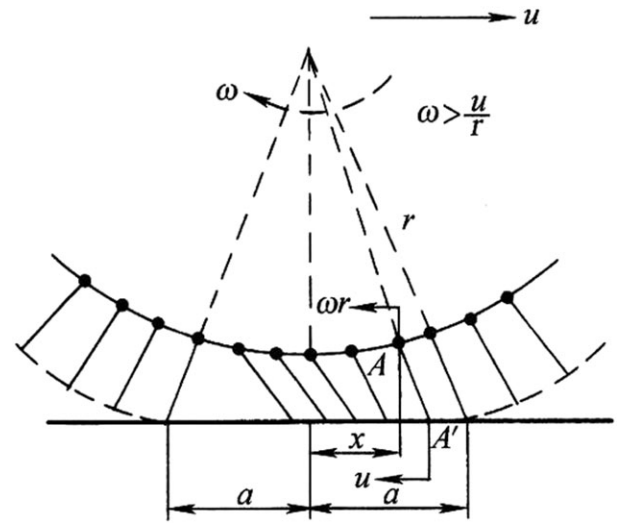


Fig. 6. Tire deformation during driving.

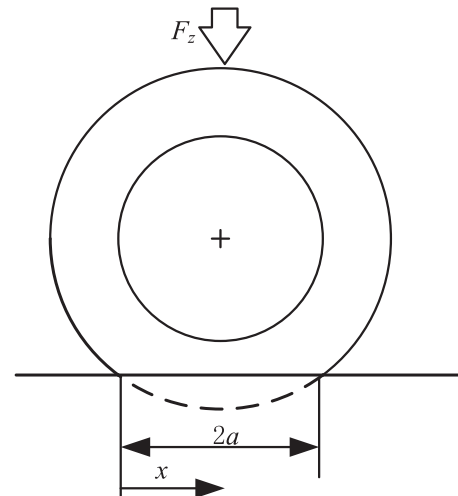


Fig. 7. Pressure distribution.

$$f_x(s, \mu) = \begin{cases} 3\mu F_z \theta_x \sigma_x \left(1 - |\theta_x \sigma_x| + \frac{1}{3} |\theta_x \sigma_x|^2\right) & \text{for } |s| \leq |s_{sl}| \\ \mu F_z \cdot \text{sign}(s) & \text{for } |s| > |s_{sl}| \end{cases} \quad (41)$$

where, $\theta_x = 2c_p a^2 / (3\mu F_z)$, $\sigma_x = s / (s + 1)$, $s_{sl} = 1 / (\theta_x - 1)$, $s = \frac{r_e \omega - v_x}{v_x}$. r_e is tire rolling radius. ω is wheel angular velocity. v_x is longitudinal speed, μ is tire/pavement friction coefficient. a is half the length of the tire contact area. F_z is vertical load of tire. c_p is tread stiffness coefficient per unit length.

(b) Lateral force f_y and self-aligning torque τ_a under pure cornering

$$f_y(\alpha, \mu) = \begin{cases} -3\mu F_z \theta_y \sigma_y \left(1 - |\theta_y \sigma_y| + \frac{1}{3} |\theta_y \sigma_y|^2\right) & \text{for } |\alpha| \leq |\alpha_{sl}| \\ -\mu F_z \cdot \text{sign}(\alpha) & \text{for } |\alpha| > |\alpha_{sl}| \end{cases} \quad (42)$$

$$\tau_a(\alpha, \mu) = \begin{cases} \mu F_z a \theta_y \sigma_y (1 - |\theta_y \sigma_y|)^3 & \text{for } |\alpha| \leq |\alpha_{sl}| \\ 0 & \text{for } |\alpha| > |\alpha_{sl}| \end{cases} \quad (43)$$

where, $\theta_y = 2c_p a^2 / (3\mu F_z)$, $\sigma_y = \tan(\alpha)$, $\alpha_{sl} = \tan^{-1}(1/\theta_y)$ is side slip angle when the tire starts to slip completely. α is side slip angle.

(c) Tire force during longitudinal and side slip combination

$$F(\alpha, s, \mu) = \begin{cases} \mu F_z \theta_y \sigma_y (1 - \rho^3) & \text{for } |\sigma| \leq |\sigma_{sl}| \\ \mu F_z \cdot \text{sign}(\alpha) & \text{for } |\sigma| > |\sigma_{sl}| \end{cases} \quad (43)$$

$$F_x = F \frac{\sigma_x}{\sigma}, F_y = F \frac{\sigma_y}{\sigma}, M_z = -t(\sigma) \cdot F_y \quad (44)$$

where, $\rho = 1 - \theta\sigma$, $\theta = 2c_p a^2 / (3\mu F_z)$, $\sigma = \sqrt{\sigma_x^2 + \sigma_y^2}$, $\sigma_x = s / (s + 1)$, $\sigma_y = (\tan \alpha) / (s + 1)$, $\sigma_{sl} = 1/\theta$, $t(\sigma) = \frac{a(1-|\theta\sigma|)^3}{3-3|\theta\sigma|+|\theta\sigma|^2}$.

(d) Tire LuGre dynamic friction model

The tire LuGre dynamic model can not only describe the Stribeck effect and the pre-slip effect of the tire friction process, but also can describe the effect of the change separation force and the friction hysteresis effect [25]. The two frictional contact surfaces are assumed to be two rigid bodies that contact each other through some so-called elastic bristles. When one of these contacts exerts a tangential force along the contact surface, the bristles will deflect as springs, and cause friction on the contact surface to

increase, as shown in Fig. 8. If the frictional force is sufficiently large, the “mane” over deflection will occur and slip occurs. Because of the unevenness of the contact surface, this “slippage” phenomenon is very random. A variable z is used to describe the average elastic deflection of the mane, and a friction model is shown as in Fig. 9.

$$F = \sigma_0 z + \sigma_1 \frac{dz}{dt} + \sigma_2 v_r \quad (45)$$

where, σ_0 is the tire longitudinal stiffness coefficient. σ_1 is the tire longitudinal damping coefficient. σ_2 is the viscous damping coefficient. z is average elastic deflection of mane, and its definition is as follows.

$$\frac{dz}{dt} = v_r - \frac{\sigma_0 |v_r|}{\theta g(v_r)} z \quad (46)$$

where, v_r is the relative velocity of contact surface, $v_r = r\omega - v$. θ is the pavement characteristics parameter. $g(v_r)$ is the sliding friction function, and its definition is as follows.

$$g(v_r) = F_C + (F_S - F_C) e^{-|v_r/v_s|^\alpha} \quad (47)$$

where, F_S is maximum static friction force. F_C is coulomp friction force. v_s is Stribeck speed. α is Stribeck exponent, $\alpha \in [0.5, 2]$.

Since the characteristics of the tire are anisotropic, longitudinal tire stiffness σ_x and lateral tire stiffness σ_y are

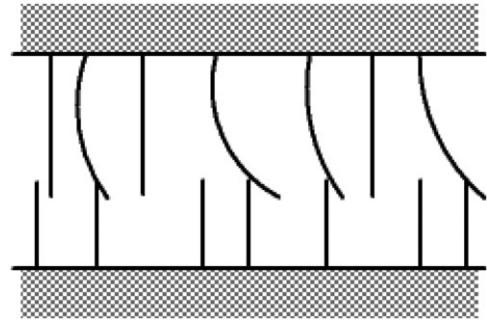


Fig. 8. “Mane” friction model.

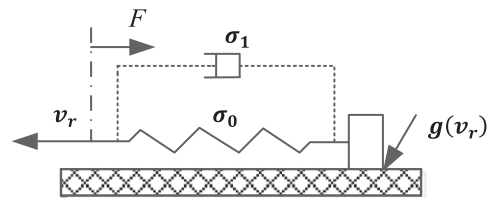


Fig. 9. LuGre dynamic friction model.

different. According to the LuGre model structure, the longitudinal and lateral components $g_{x,y}$ of the sliding friction force $g(v_r)$ between the tires/road surface are positive and can be written as follows.

$$g_{x,y}(v_r, v_{rx,y}) = \left| \frac{v_{rx,y}}{v_r} \right| g(v_r) \quad (48)$$

The final deformation equation of bristle deformation z under longitudinal and lateral joint conditions can be obtained as follows.

$$\frac{\partial z_{x,y}(\zeta, t)}{\partial t} = v_{rx,y} - \frac{\sigma_{0x,y}|v_r|}{g(v_r)} z_{x,y}(\zeta, t) - r|\omega| \frac{\partial z_{x,y}(\zeta, t)}{\partial \zeta} \quad (49)$$

For steady state, the formula in equation 49 has $\partial z_{x,y}(\zeta, t)/\partial t = 0$, the steady state analytical solution can be

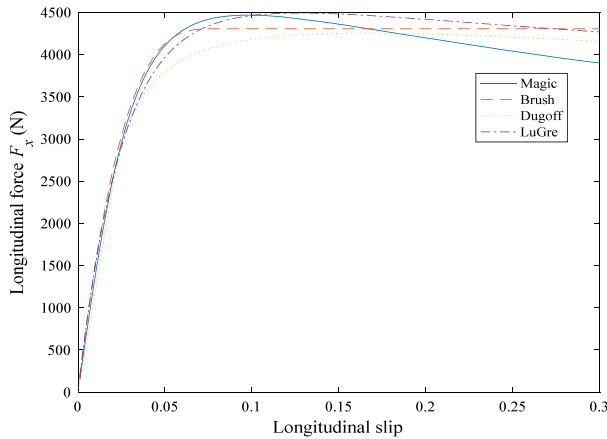


Fig. 10. Longitudinal force comparison of each tire. [Color figure can be viewed at wileyonlinelibrary.com]

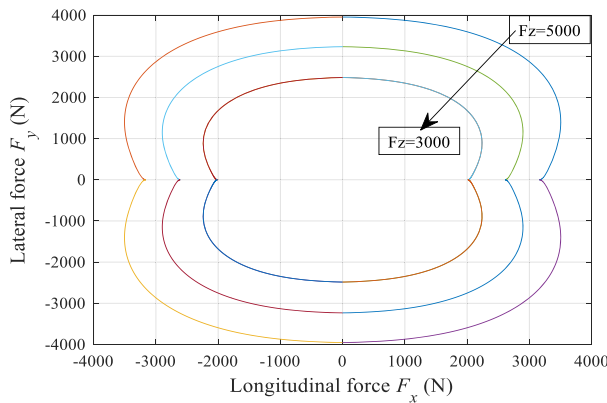


Fig. 11. Magic formula tire ellipse. [Color figure can be viewed at wileyonlinelibrary.com]

obtained, and then the expressions of longitudinal / lateral steady tire force and self-aligning torque can be obtained.

According to the above tire model (205/55R16), the simulation comparisons were shown in Figs 10–13. Compared with the exact formula of the magic formula tire, we can see the accuracy of the tire LuGre steady state model is very satisfactory. Figs 10 and 11 show the elliptic based on magic tire formula, in which the vertical loads of the wheels are 5000 N, 4000 N, 3000 N, respectively, and the characteristics of the force of the tire and the ground are shown. Fig. 12 shows θ influence on road surface friction, and that the friction coefficient of the pavement is characterized by θ . Through the process of emergency braking as Fig. 13, we can see using the LuGre dynamic friction tire model is preferable because it reflects the tire response characteristics. This cannot be seen in the steady state tire model. Therefore, the LuGre model is chosen for dynamic simulation in the paper.

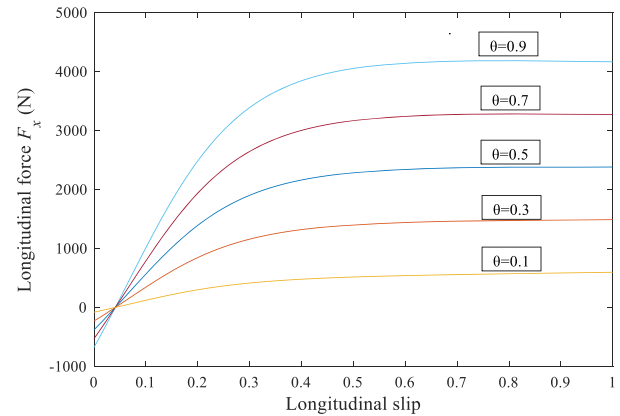


Fig. 12. θ influence on adhesion coefficient. [Color figure can be viewed at wileyonlinelibrary.com]

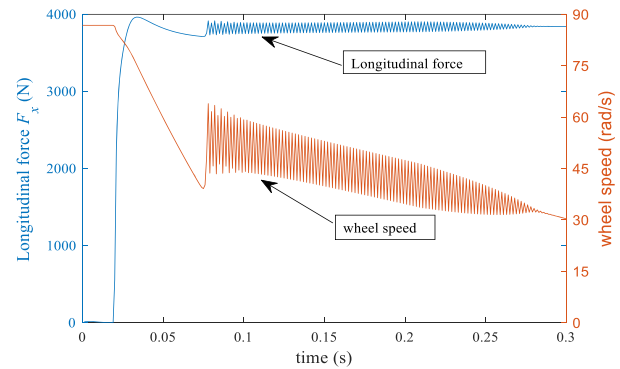


Fig. 13. Dynamic response under emergency braking. [Color figure can be viewed at wileyonlinelibrary.com]

2.5 Dynamic simulation results comparison

In order to verify the accuracy of the model and the development of the chassis integrated control system, a winter test was carried out at the Heihe proving ground. Fig. 14 is the main test equipment and test site photos. The experimental vehicle is a Mazda6, and the test system includes four Huba 511 series oil pressure sensors, strain gauge, GPS RT3100 inertial navigation measurement system, NI PXI data acquisition system, etc. Test methods include asphalt, snow and ice, double lane, J turn, and serpentine conditions, etc. Fig. 15 is the yaw angular velocity and serpentine simulation results. Fig. 16 shows the rolling angle and simulation results. We can see that the accuracy of the model is satisfactory.



Fig. 14. On-board test system. [Color figure can be viewed at wileyonlinelibrary.com]

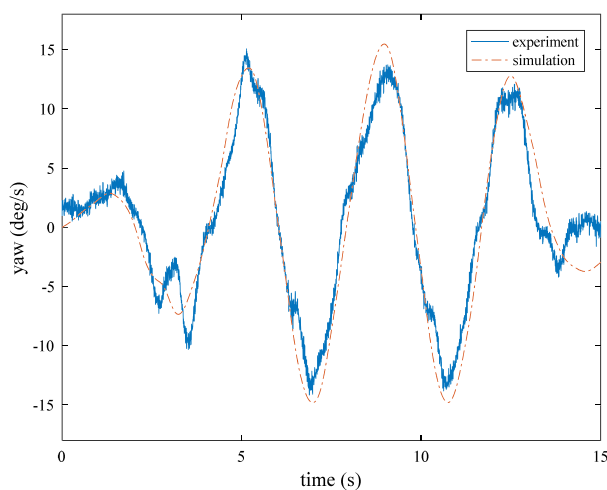


Fig. 15. Comparison of yaw angular velocity. [Color figure can be viewed at wileyonlinelibrary.com]

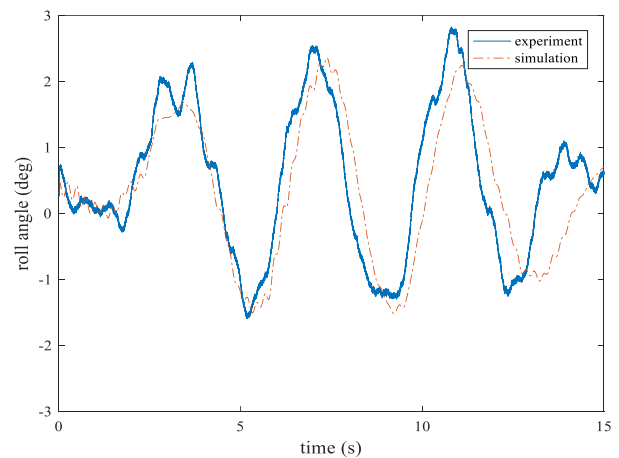


Fig. 16. Roll angle comparison. [Color figure can be viewed at wileyonlinelibrary.com]

III. AFS/ESP INTEGRATED CONTROL SYSTEM

3.1 Ideal state calculation

In order to calculate the vehicle ideal state, a linear two degrees of freedom model is established, which includes lateral motion and yaw motion [26–29], and is shown in Fig. 17. Vehicle motion equations are expressed as follows.

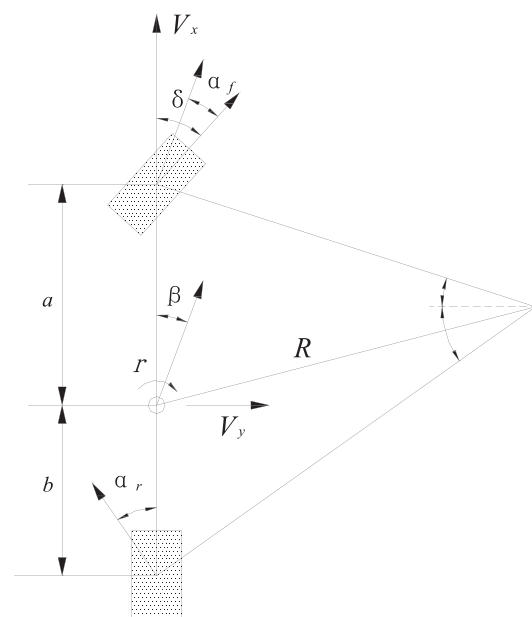


Fig. 17. Linear two degrees of freedom model.

$$\begin{cases} mV_x(\dot{\beta} + r) = F_{yf} + F_{yr} \\ I_{zz}\dot{r} = F_{yf} \cdot a - F_{yr} \cdot b \end{cases} \quad (50)$$

where, $\begin{cases} F_{yf} = C_{af} \cdot a_f \\ F_{yr} = C_{ar} \cdot a_r \end{cases}$, $\begin{cases} a_f = \delta_f - \frac{V_y + a \cdot r}{V_x} \\ a_r = -\frac{V_y - b \cdot r}{V_x} \end{cases}$, and

substituting for equation 50, then.

$$\begin{bmatrix} \dot{\beta} \\ \dot{r} \end{bmatrix} = \begin{bmatrix} a_{11} & a_{12} \\ a_{21} & a_{22} \end{bmatrix} \begin{bmatrix} \beta \\ r \end{bmatrix} + \begin{bmatrix} b_1 \\ b_2 \end{bmatrix} \delta \quad (51)$$

where, $a_{11} = \frac{-2C_{af}-2C_{ar}}{mV_x}$, $a_{12} = -1 + \frac{2C_{ar}b-2C_{af}a}{mV_x^2}$, $a_{21} = \frac{2C_{ar}b-2C_{af}a}{I_{zz}}$, $a_{22} = \frac{-2C_{af}a^2-2C_{ar}b^2}{I_{zz}V_x}$, $b_1 = \frac{2C_{af}}{mV_x}$, $b_2 = \frac{2C_{af}a}{I_{zz}}$.

Thus, the lateral side slip angle and yaw angular velocity can be obtained in steady circumferential motion.

$$\begin{cases} \beta_{ss} = \frac{[2bLC_{af}C_{ar} - mV_x^2aC_f]}{2C_{af}C_{ar}L^2 - mV_x^2(aC_{af} - bC_{ar})} \delta \\ r_{ss} = \frac{2LC_{af}C_{ar}V_x}{2C_{af}C_{ar}L^2 - mV_x^2(aC_{af} - bC_{ar})} \delta \end{cases} \quad (52)$$

When doing circular motion, the yaw speed of the vehicle is limited by the condition of the road surface adhesion, that is, there is the maximum allowable yaw angular velocity. The calculation process is as follows: the lateral acceleration of the vehicle center of mass is $a_y = V_x r + \dot{V}_y$, where, $V_y = V_x \tan \beta$. Then a_y can be expressed as $a_y = V_x r + \dot{V}_x \tan \beta + \frac{V_x \dot{\beta}}{\sqrt{1 + \tan^2 \beta}}$. The lateral acceleration at the tire attachment limit must be met $|a_y| \leq \mu \cdot g$. The maximum yaw rate can be expressed by the approximate formula $r_{up\lim} = 0.85 \cdot \left| \frac{\mu \cdot g}{V_x} \right|$. In this way, the ideal yaw rate r_d is as follows.

$$r_d = \min[|r_{ss}|, |r_{up\lim}|] \cdot \text{sign}(\delta) \quad (53)$$

The empirical formula of limit side slip angle is $\beta_{up\lim} = \tan^{-1}(0.02\mu g)$, so the ideal side slip angle is as follows.

$$|\beta_d| = \min[|\beta_{ss}|, |\beta_{up\lim}|] \quad (54)$$

3.2 AFS control logic

The tracking error is $e_c = r - r_d$ and its rate is $\dot{e}_c = \dot{r} - \dot{r}_d$. The sliding surface can be defined as $s = e_c$. The sliding mode dynamics of the system is as follows.

$$\dot{s} = -\lambda s \text{ or } \dot{r} - \dot{r}_d = -\lambda(r - r_d) \quad (55)$$

where, λ is positive constant. We take the equation 55 into the equation 51.

$$a_{21}\beta + a_{22}r + b_2\delta - \dot{r}_d = -\lambda(r - r_d) \quad (56)$$

Then, the control rule is as follows.

$$\delta = \frac{1}{b_2} [-a_{21}\beta - a_{22}r + \dot{r}_d - \lambda(r - r_d)] - \chi \text{sgn}(s) \quad (57)$$

where, χ is the control gain, which determines the speed of the system when it reaches the slip surface. Then the additional input angle of AFS is $\Delta\delta = \rho_c(\delta - \delta_d)$, ρ_c is the coordination control parameter, δ_d is front wheel desired angle by the driver.

3.3 ESP and coordinated control algorithm

The switching control algorithm is adopted in this paper. The compensation torque ΔM_z obtained by the ESP control system is as follows.

$$\Delta M_z = (1 - \rho_c)(k_1|r - r_d| - k_2|\beta - \beta_d|) \quad (58)$$

For convenient handle in engineering, setting $\beta_d = 0$, value of ρ_c is shown in the following formula.

$$\begin{cases} \rho_c = 1 & |\kappa_1\dot{\beta} + \kappa_2\beta| < B_1 \\ \rho_c = \frac{B_2 - |\kappa_1\dot{\beta} + \kappa_2\beta|}{B_2 - B_1} & B_1 \leq |\kappa_1\dot{\beta} + \kappa_2\beta| \leq B_2 \\ \rho_c = 0 & |\kappa_1\dot{\beta} + \kappa_2\beta| > B_2 \end{cases} \quad (59)$$

where κ_1, κ_2, B_1 and B_2 are positive constants. They represent the definition of a stable region and can be obtained by experimentation or trial.

The calculation of coordinated control parameter ρ_c is shown in Fig. 18.

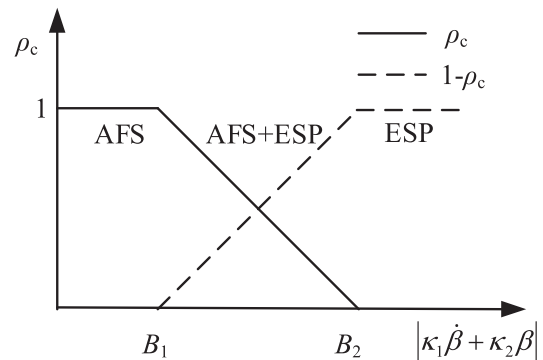


Fig. 18. Coordination control characteristics.

The simple selection principle of the active braking wheel is shown in Table I. In this paper, a simple control rule is used, that is, this control method can provide the compensation torque well so as to control the vehicle stability.

According to the friction circle theory of tire mechanics, the longitudinal slip ratio of wheel increases Δi_s , the

Table I. Simple principles for selection of brake wheels.

δ	$e_c(r)$	Direction of the steering wheel	Steering characteristics	Brake wheel selection
+	+	right	oversteer	Left front wheel
+	-	right	understeer	Right rear wheel
-	+	left	oversteer	Right front wheel
-	-	left	understeer	Left rear wheel

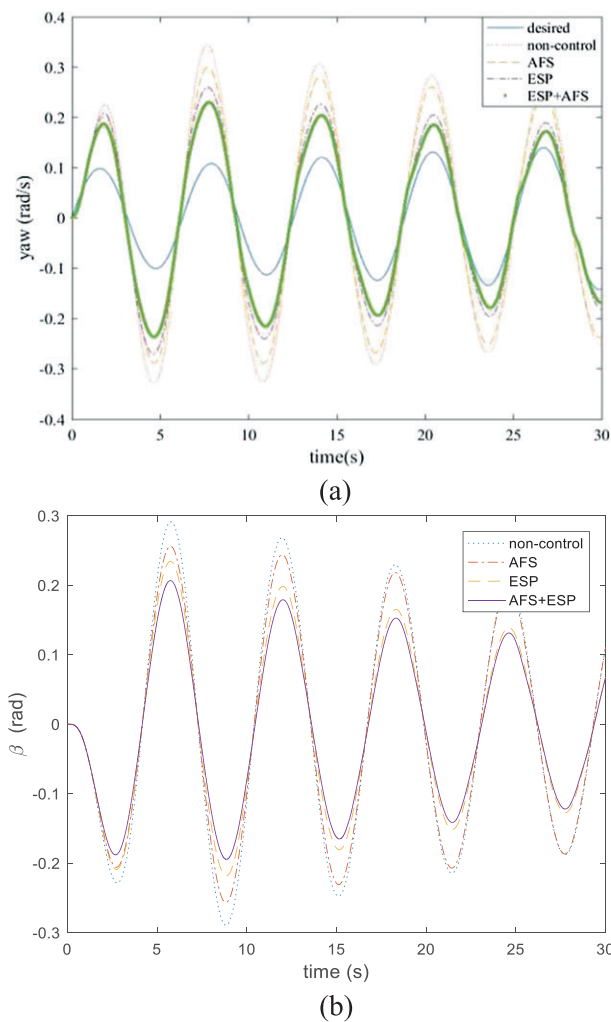


Fig. 19. Serpentine simulation of high friction road. [Color figure can be viewed at wileyonlinelibrary.com]

longitudinal force increases ΔF_{xi} , while the lateral force decreases ΔF_{yi} . According to Table I, if there is oversteer and it is necessary to brake on the outside front wheel, the yaw moment ΔM_z is obtained as follows.

$$\Delta M_z = \Delta F_{xi} \cdot \left(\frac{T_w}{2} \cos \delta + a \cdot \sin \delta \right) - \Delta F_{yi} \left(a \cdot \cos \delta - \frac{T_w}{2} \sin \delta \right) \quad (60)$$

When understeer occurs, the inner rear wheel is braked, and the yaw moment ΔM_z is obtained as follows.

$$\Delta M_z = \Delta F_{xi} \cdot \frac{T_w}{2} - \Delta F_{yi} \cdot b \quad (61)$$

After simplifying, there is $\Delta F_{xi} = \frac{2\Delta M_z}{T_w}$. In combination with the tire model, the relation between ΔM_z and Δi_s

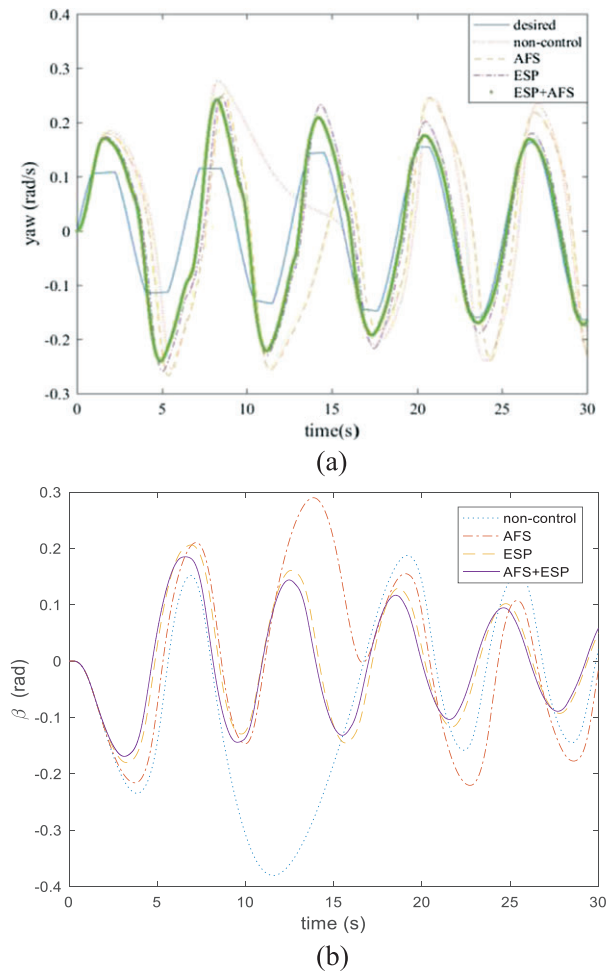


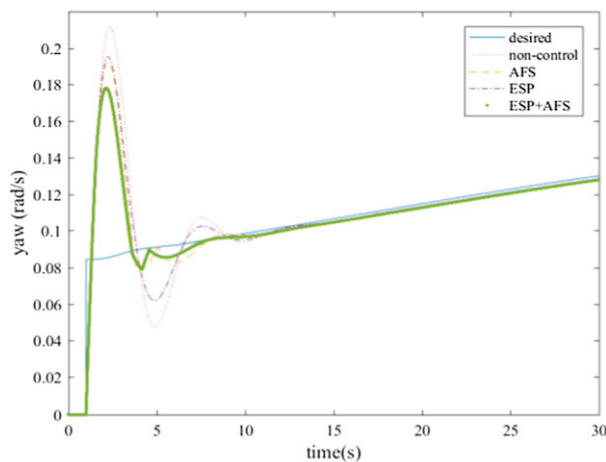
Fig. 20. Serpentine simulation of low friction road. [Color figure can be viewed at wileyonlinelibrary.com]

can be obtained. Then the increment P_b of the braking pressure can be obtained approximately as $P_b = k_b \Delta F_{xi}$.

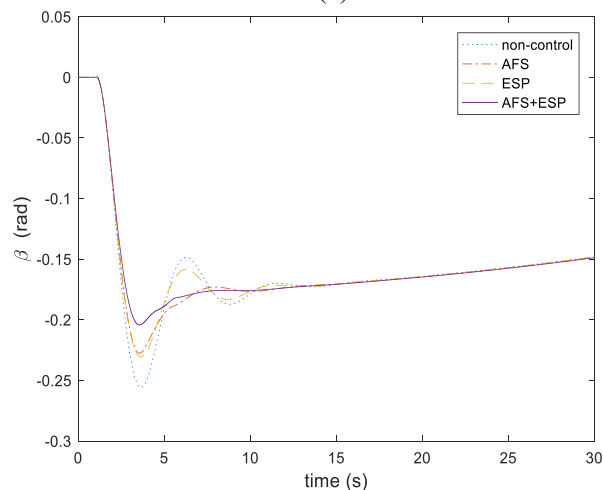
3.4 Simulation comparison

According to the above AFS, ESP and integrated control logic, simulation analysis is carried out. The Serpentine simulation was compared, Fig. 19 is on high adhesion coefficient road ($\mu=0.9$, initial speed $u_0=100$ km/h), it can be seen that coordinated control is the closest to the desired value. The curves in Figs 19 and 20 are desired yaw rate, non-control, only AFS control, only ESP control, and AFS/ESP coordinated control correspondingly. Fig. 20 is on the low adhesion coefficient road ($\mu=0.2$, initial speed $u_0=60$ km/h), and it can be seen that in the low friction coefficient road, if no control is applied, the car will be

unstable. And the effect of coordinated control is similar to ESP control. Figs 21 ($\mu=0.9$, initial speed $u_0=100$ km/h) and 22 ($\mu=0.2$, initial speed $u_0=60$ km/h) are respectively step angle input simulation comparisons on high/low adhesion pavement coefficients. It can be seen that the control effect order from weak to strong is AFS→ESP→AFS+ESP. If the vehicle is in the stable region, AFS should be preferred, because the ESP will make the braking system involved, which will make the vehicle comfort and fuel economy become poor. So in the control process, we should let AFS play a role first, if AFS is not sufficient for stability control of the vehicle, let ESP be the intervention. If it is urgent to turn sharply, we can make the ESP a direct intervention.

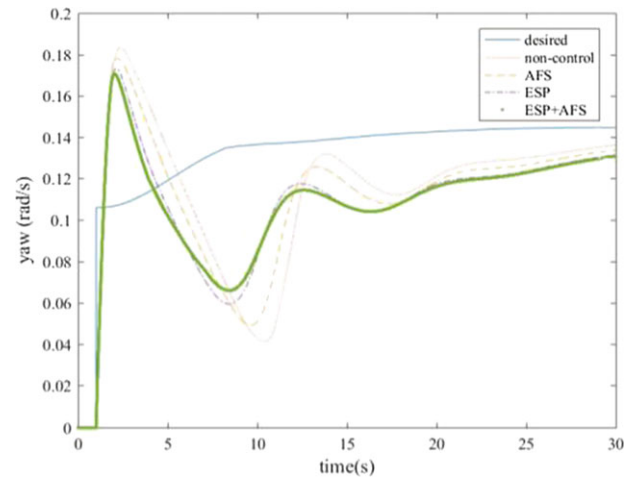


(a)

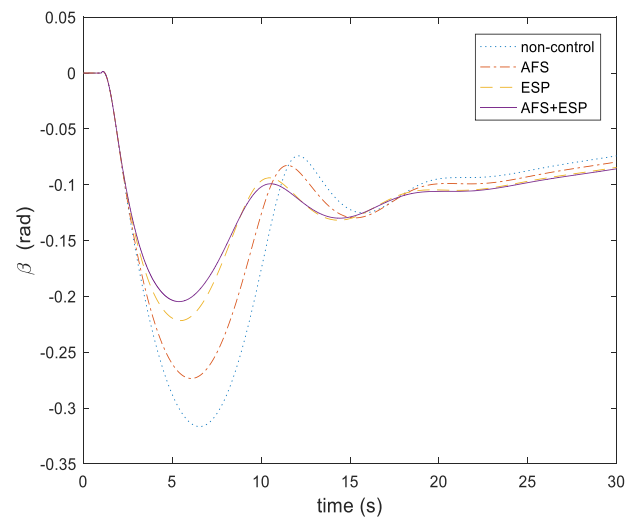


(b)

Fig. 21. Step angle input of high friction road. [Color figure can be viewed at wileyonlinelibrary.com]



(a)



(b)

Fig. 22. Step angle input of low friction road. [Color figure can be viewed at wileyonlinelibrary.com]

IV. CONCLUSIONS

The multi-degree of freedom nonlinear dynamic vehicle model including body movement, wheel movement and electronically controlled hydraulic power steering system was built firstly. A comparative study was conducted with the magic formula tire model, Dugoff tire model, brush tire model, and LuGre dynamic friction tire model and the steady state tire model based on LuGre. A comparative study was conducted between the simulation results and the real vehicle test results, during which the precision of the model was verified. Then based on the vehicle dynamics model, an AFS controller was designed based on sliding mode variable structure control, and the AFS and ESP integrated coordination controller was proposed. The sinusoidal and steering angle step input simulation analysis was proposed based on a multi-DOF vehicle model and nonlinear tire model. The simulation results show that, compared with the action of AFS or ESP alone, the vehicle response characteristics are better under a coordinated control strategy, so that the method can obviously improve the handling stability and safety of the vehicle.

REFERENCES

1. Aripin, M. K., Y. M. Sam, and A. D. Kumeresan, "A yaw rate tracking control of active front steering system using composite nonlinear feedback," *Commun. in Comput. Inform. Sci.*, Vol. 402, pp. 231–242 (2013).
2. Zheng, B., and S. Anwar, "Yaw stability control of a steer-by-wire equipped vehicle via active front wheel steering," *Mechatronics*, Vol. 19, No. 6, pp. 799–804 (2009).
3. Krishna, S., S. Narayanan, and S. D. Ashok, "Fuzzy logic based yaw stability control for active front steering of a vehicle," *J. Mech. Sci. Technol.*, Vol. 28, No. 12, pp. 5169–5174 (2014).
4. Yim, S., W. Cho, and J. Yoon, "Optimum distribution of yaw moment for unified chassis control with limitations on the active front steering angle," *Int. J. Automotive Technol.*, Vol. 11, No. 5, pp. 665–672 (2010).
5. Nam, K., S. Oh, and H. Fujimoto, "Robust yaw stability control for electric vehicles based on active front steering control through a steer-by-wire system," *Int. J. Automotive Technol.*, Vol. 13, No. 7, pp. 1169–1176 (2012).
6. Fujimoto, H., and K. Maeda, "Optimal yaw-rate control for electric vehicles with active front-rear steering and four-wheel driving-braking force distribution," *IEEE Trans. Sensors Micromachines*, Vol. 131, No. 131, pp. 6514–6519 (2010).
7. Cairano, S. D., H. E. Tseng, and D. Bernardini, "Vehicle yaw stability control by coordinated active front steering and differential braking in the tire side slip angles domain," *IEEE Trans. Control Syst. Technol.*, Vol. 21, No. 4, pp. 1236–1248 (2013).
8. Elmarakbi, A., C. Rengaraj, and A. Wheatley, "The influence of electronic stability control, active suspension, driveline and front steering integrated system on the vehicle ride and handling," *Global J. Res. Eng.*, Vol. 13, No. 1, pp. 1–14 (2013).
9. Choi, M., and S. B. Choi, "MPC for vehicle lateral stability via differential braking and active front steering considering practical aspects," *Proc. Inst. Mech. Eng. Part D, J. Automobile Eng.*, Vol. 230, No. 4, pp. 1–11 (2016).
10. Guo, J., L. Chu, and H. Liu, "Integrated control of active front steering and electronic stability program," *IEEE Int. Conf. Advanced Comput. Control*, Shenyang, China, pp. 449–453 (2010).
11. Marar, A., D. Ginoya, and S. B. Phadke, "Robust yaw stability control based on disturbance observer using active front steering," *IEEE Int. Conf. Ind. Instrumentation and Control*, Pune, India, pp. 1367–1372 (2015).
12. Saikia, A. and C. Mahanta, "Vehicle stability enhancement using sliding mode based active front steering and direct yaw moment control," *IEEE Control Conf.*, Guwahati, India, pp. 378–384 (2017).
13. Yang, I., S. Byun, and B. Seo, "Integrated control systems of active front steering and direct yaw moment control using dynamic inversion," *IEEE Intell. Vehicles Symposium*, Gold Coast, Australia, pp. 1303–1306 (2013).
14. Sun, T., H. Guo, and J. Y. Cao, "Study on integrated control of active front steering and direct yaw moment based on vehicle lateral velocity estimation," *Math. Probl. Eng.*, Vol. 2013, No. 12, pp. 707–724 (2013).
15. Dadras, S., H. R. Momeni, and S. Dadras, "Adaptive control for ship roll motion with fully unknown parameters," *IEEE Int. Conf. Control and Automation*, Christchurch, New Zealand, pp. 270–274 (2009).
16. Dadras, S., S. Dadras, and H. R. Momeni, "Linear matrix inequality based fractional integral sliding-mode control of uncertain fractional-order nonlinear systems," *J. Dyn. Syst., Meas., Control*, Vol. 139, pp. 11, 111003 (2017).
17. Ghanavati, M., A. Chakravarthy, and P. P. Menon, "Analysis of automotive cyber-attacks on highways using partial differential equation models," *IEEE Trans. Control Network Syst.*, Vol. PP, No. 99, pp. 1–11 (2017).
18. Solmaz, S., M. Corless, and R. Shorten, "A methodology for the design of robust rollover prevention controllers for automotive vehicles with active steering," *Int. J. Control*, Vol. 80, No. 11, pp. 1763–1779 (2007).
19. Chiu, J., S. Solmaz, M. Corless, and R. Shorten, "A methodology for the design of robust rollover

- prevention controllers for automotive vehicles using differential braking,” *Int. J. Vehicle Autonomous Syst.*, Vol. 8, No. 2/3, pp. 146–170 (2010).
20. Boada, B. L., M. J. L. Boada, and V. Díaz, “Fuzzy-logic applied to yaw moment control for vehicle stability,” *Veh. Syst. Dyn.*, Vol. 43, No. 10, pp. 753–770 (2005).
 21. Proca, A. B., and A. Keyhani, “Identification of power steering system dynamic models,” *Mechatronics*, Vol. 8, No. 98, pp. 255–270 (1998).
 22. Dugoff, H., P. S. Fancher, and L. Segel, “Analysis of tire traction properties and their influence on vehicle dynamic performance,” *Society of Automotive Engineers (SAE) Trans. (SAE paper No. 700377)*, Vol. 79, pp. 341–366 (1970).
 23. Pacejka, H. B., *Tyre and Vehicle Dynamics*, Butterworth-Heinemann, Oxford, United Kingdom (2006).
 24. Erdogan, G., L. Alexander, and R. Rajamani, “Estimation of tire-road friction coefficient using a novel wireless piezoelectric tire sensor,” *IEEE Sens. J.*, Vol. 11, No. 2, pp. 267–279 (2011).
 25. Tsiotras, P., E. Velenis, and M. Sorine, “A LuGre tire friction model with exact aggregate dynamics,” *Vehicle System Dynamics*, Vol. 42, No. 3, pp. 195–210 (2004).
 26. Tiwari, P. M., S. Janardhanan, and M. Un-Nabi, “Spacecraft anti-unwinding attitude control using second-order sliding mode,” *Asian J. Control*, Vol. 20, No. 1, pp. 455–468 (2018).
 27. Rajamani, R., *Vehicle Dynamics and Control*, Springer US (2012).
 28. Jin, X. J., G. Yin, Y. Li, *et al.*, “Stabilizing vehicle lateral dynamics with considerations of state delay of AFS for electric vehicles via robust gain-scheduling control,” *Asian J. Control*, Vol. 18, No. 1, pp. 89–97 (2016).
 29. Yu, H., S. Taheri, J. Duan, *et al.*, “An integrated cooperative antilock braking control of regenerative and mechanical system for a hybrid electric vehicle based on intelligent tire,” *Asian J. Control*, Vol. 18, No. 1, pp. 55–68 (2016).



Xiaobin Fan received his Ph.D. in Mechanical Engineering from the University of Science and Technology Beijing, Beijing, China, in 2007. He works at the School of Mechanical and Power Engineering, Henan Polytechnic University. His current research interests include automotive system dynamics and control, noise, and vibration control.



Zixiang Zhao is currently a postgraduate student of Henan Polytechnic University, Jiaozuo, China. His current research interests include vehicle dynamics and control.